Geothermal Energy

RESEARCH Open Access

Deep structure and geothermal resource effects of the Gonghe basin revealed by 3D magnetotelluric

Yi Yang[1,2,3], Jie Zhang[1,3], Xingchun Wang[1,3*], Mingxing Liang[1,3], Dewei Li[6], Meng Liang[1,3], Yang Ou[1,3], Dingyu Jia[1,3], Xianchun Tang[4] and Xufeng Li[5]

*Correspondence:
wxingchun@mail.cgs.gov.cn

[1] The Institute of Geophysical and Geochemical Exploration, Langfang 065000, China
[2] Chengdu University of Technology, Chengdu 610059, China
[3] Key Laboratory of Geophysical Electromagnetic Detection Technology, Ministry of Natural Resources, Langfang 065000, China
[4] Chinese Academy of Geological Sciences, Beijing 100081, China
[5] Center For Hydrogeology and Environmental Geology, CGS, Baoding 071051, China
[6] Center For Chengdu Geological Survey, CGS, Chengdu 610081, China

Abstract

In order to better understand the crustal shortening and orogenic uplift in the northeastern margin of the Tibetan Plateau, as well as the geothermal resource effects formed during this process, we used ModEM software to perform 3D MT imaging on broadband magnetotelluric survey points deployed at 710 points in the Gonghe Basin and its surrounding areas. The resistivity model suggests that the Gonghe Basin exhibits a low–high–low overall electrical structure, with high conductivity widely distributed in the middle and lower crust. The resistivity model also reveals a significant discontinuity between high and low resistivity blocks at various depths in the upper and middle crust. These discontinuities are align with the faults observed on the surface related to strong crustal fluctuations, which are connected to high conductors in the middle and upper crust. Using empirical formulas for high-temperature and high-pressure testing of granite, it is estimated that the melting volume of these high conductors ranges from 3 to 43%, demonstrating good "plasticity". These high conductors can act as detachment layers for crustal shortening and deformation during the expansion of the Tibetan Plateau towards the northeast edge and can continuously conduct heat energy upwards, creating a high thermal background in the Gonghe Basin.

Keywords: Tibetan Plateau, Gonghe Basin, Magnetotelluric, 3D inversion, Melting, Structure, Geothermal

Introduction

Approximately 50 Ma ago, the collision between the Indian Plate and the Eurasian plate forced the uplift of the Tibetan Plateau. Since the collision, the tectonic shortening between the two plates has amounted to 2000 km (Clark and Royden 2000; Yuan et al. 2013). This has led to severe crustal deformation (Tapponnier et al. 2001), resulting in the unique crustal structure and high geothermal background of the Tibetan Plateau. Scholars have proposed various deformation mechanisms and dynamic models to explain the uplift of the Tibetan Plateau (Clark and Royden 2000; Tapponnier et al. 2001; Dewey and Burke 1973). Evidence from disciplines such as geophysics and deformation

measurement (Shen et al. 2001; Wang et al. 2016a, 2013; Chen et al. 2004a; Liu et al. 2014; Sun et al. 2012) provides varying degrees of support for these deformation mechanisms and dynamic hypotheses. However, a specific deformation model struggles to account for the deformation of the entire Tibetan Plateau continent. Different regions or blocks may predominantly exhibit one deformation mode, while also featuring other deformation modes (Liu et al. 2014; Replumaz and Tapponnier 2003; Xu et al. 2010; Li et al. 2021). The debate about the uplift and dynamic mechanism of the Tibetan Plateau continues, and the unclear deep structure and process contribute to the ongoing controversy over the formation mechanism, tectonic model, and deformation mode of the Tibetan Plateau (Pan et al. 2020).

The Gonghe Basin is located at the junction of the Qinling–Qilian–Kunlun orogenic belt on the northeastern margin of the Tibetan Plateau, where the original Tethys and ancient Tethys systems overlap (Zhang et al. 2006; Yang et al. 2018). It records complex tectonic, magmatic and metamorphism events, making it an ideal window for studying the deformation model and tectonic evolution of the northeastern margin of the Tibetan Plateau (Yun et al. 2020). The internal structure of the Earth, determined through geophysical methods, provides information most closely related to deep material migration, crustal lithosphere deformation and deep dynamic processes (Lü et al. 2022), However, the medium attributes in the crust and mantle, caused by the material migration and tectonic deformation history in the Earth's evolution process, are directly related to the Geodynamics characteristics (Silver 1996). The seismic wide-angle reflection detection results show that the internal structure of the crust in the northeastern margin of the Tibetan Plateau varies greatly across different geological tectonic blocks, with clear low-velocity anomaly structures in the crust (Zhang et al. 2008). The tomographic inversion results suggest widespread low P-wave velocity anomalies in the lower crust of the northeastern margin of the Tibetan Plateau (Zhou et al. 2012). The velocity structure of the crust and upper mantle exhibits significant lateral changes along the profile, and the crustal thickness gradually increases southward in a stepped manner (Xue et al. 2003; Pan et al. 2017). The average P-wave velocity in the lower crust and upper mantle is relatively low (Guo et al. 2004), suggesting that crustal thickening may predominantly occur in the middle and lower crust (Wang et al. 2014; Xiao and Gao 2017). The continuous distribution of low-velocity layers in the middle and lower crust may be related to subterranean melting (Xia et al. 2021). The results of magnetotelluric sounding in Tibetan Plateau (Bai et al. 2010; Chen et al. 2004b; Sun et al. 2003; Wang et al. 2017; Wei et al. 2006; Xiao et al. 2013; Gao et al. 2018, 2020) also reveal high-conductivity layers with varying depths and sizes in the crust of vast areas inside and on the margin of Tibetan Plateau. These observations indicate that the material in the middle and lower crust of these areas is weak in physical properties.

Deep geophysical explorations have shown that the crustal thickening on the northeastern edge of the Tibetan Plateau is characterized by low P-wave velocity and low resistivity (Zhang et al. 2008; Zhou et al. 2012; Jia et al. 2019; Gao et al. 2018, 2020). The Maduo-Gonghe deep reflection seismology results show that the bottom interface of the upper crust (C1) is missing in the Gonghe Basin, and the apparent velocity of the middle and lower crust is low, exhibiting velocity plastic deformation characteristics(Jia et al. 2019). The western Gonghe Basin demonstrates clear characteristics of low density,

low-gravity anomaly, low velocity and low resistivity, indicating the presence of low-density materials with high conductivity in the lower crust (Gao et al. 2018, 2020; Zhang et al. 2021). The inversion of the interface-based on aeromagnetism and gravity indicates that the Gonghe Basin is located in the raised area of the Moho surface and the gradually changing area of the Curie surface, and there is a clear coupling relationship between these two interfaces and the distribution of geothermal flow (Zhao et al. 2020). In recent years, multiple drilling wells (GRl, ZR2, GH01) constructed in the Gonghe Basin have all encountered high-temperature rock masses (Zhang et al. 2018a, 2019), with temperatures above 180 ℃ at depths of 3000 m. The geothermal flow measurement based on boreholes shows that the average geothermal flow in the Gonghe Basin is 102.2 mW/m^{-2}, significantly higher than the average geothermal flow in mainland China of 60.4 mW/m^{-2} (Zhang et al. 2018a), indicating that the high geothermal flow background in the Gonghe Basin is closely related to deep structures.

In recent years, many scholars have conducted geophysical exploration research on the geothermal energy in the Gonghe Basin (Gao et al. 2020, 2018; Zhao et al. 2020; Zhang et al. 2019, 2018b), focusing on the characteristics of geothermal flow (Zhang et al. 2018a). These studies have achieved some understanding of the distribution of dry hot rock masses and the potential of geothermal resources of dry hot rocks (Xu et al. 2018). However, consensus has not been reached regarding the reasons for the high heat flow in the basin (Yan 2015; Tang et al. 2020; He et al. 2023). The reason for this discrepancy is that the research methods employed in these studies were relatively narrow, and the deep state of matter—closely related to the high thermal background of the Gonghe Basin—has not been fully described, thereby limiting the evaluation, development and utilization of geothermal resources in the Gonghe Basin.

Electromagnetic exploration plays a unique and important role in the investigation of geothermal resource over the world (Pinã et al. 2014; Patro 2017). On one hand, it can reveal the correlation between the resistivity of underground media and key parameters such as porosity, permeability, salinity, and temperature (Flores et al. 2022; Pavez et al. 2022). On the other hand, there are significant differences in the electrical resistivity of different parts of geothermal systems, such as thermal channels, heat sources (Cheng et al. 2022), thermal reservoirs, and cap rocks (Tan et al. 2021). Magnetotelluric (MT) method is the most effective way to determine the heat source of deep high-temperature geothermal systems (Gao et al. 2018). At present, MT have been widely used in volcanic geothermal structure investigation (Miensopust et al. 2014; Hashimoto et al. 2019) and hydrothermal fluid circulation (Amatyakula et al. 2016; Wang et al. 2023). Electromagnetic data can also be used for geothermal field prediction (Spichak et al. 2011), geothermal development and fracturing monitoring (Peacock et al. 2012; Abdelfettah et al. 2018; Darnet 2004; Darnet et al. 2020). These detection examples indicate that electromagnetic methods have shown good adaptability and effectiveness in the exploration of geothermal resources, and are playing an increasingly important role.

In this study, to more comprehensively study the deep structure of the Gonghe Basin and its geothermal resource effect, we utilized broadband frequency magnetotelluric survey points covering the entire Gonghe Basin. We carry out a 3D MT imaging survey of the middle and deep parts of the entire basin, discussed the characteristics of basin's electrical structure, and analyzed the typical electrical profile in combination with

seismic wave velocity profile and gravity anomaly. Finally, based on the current understanding of high-temperature and high-pressure petrophysical experiments, we provide some interpretations and discussions on the structure and state of matter of the middle and deep parts of the Gonghe Basin.

Geological setting

Gonghe Basin is situated at the junction of Qinling–Qilian–Kunlun Orogenic belt (Fig. 1a, b) (Shi and Zhang 1982; Zhang et al. 2004). Structurally, the Gonghe Basin is a typical Cenozoic intermountain basin controlled by Kunlun Fault and Altyn Tagh Fault (Feng et al. 2002) (Fig. 1a). Multiple secondary thrust strike-slip faults form the boundary of the Gonghe Basin between these two primary strike-slip faults, with Qinghai Nan Shan Fault as the boundary to the north, Ela Shan Fault to the west, Kunlun Fault to the south, and Duohemao Fault to the east (Fig. 1b). These faults have played an important role in shortening and uplifting the basin. In the basin, the Qinghai Nan Mount, Gonghe Nan Mount and Wali Guan uplift belt (Fig. 2a) within the basin all resulted from tectonic shortening deformation following the collision between India and Eurasia during the Cenozoic era (Craddock et al. 2014), making them are of great significance in studying the uplift model and tectonic evolution of the northeastern Tibetan Plateau (Su et al. 2017).

A digital elevation model (DEM) (Aster GDEM, http://datamirror.csdb.cn/admin/datademMain.jsp) reveals the landscape structural characteristics of "two mountains and one basin" in Gonghe Basin and its adjacent areas (Fig. 2). QHNS and GHNS in the near NW direction enclose the Gonghe basin, aligning with the direction of NE–SW principal stress in the basin (Craddock et al. 2014). GPS observations around the basin also support this conclusion and provide more detailed deformation characteristics of the basin. We selected the GPS velocity field of Ref. (Zheng et al. 2017) and set the GPS

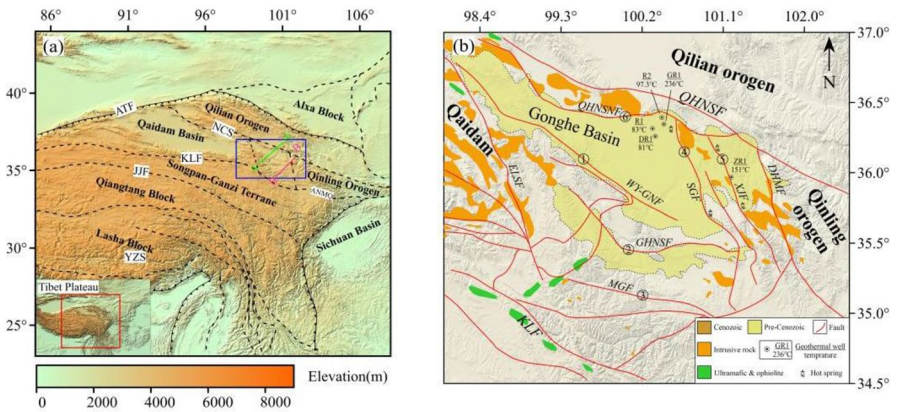

Fig. 1 Tectonic setting of Gonghe Basin and Tibetan Plateau. **a** Tectonic setting around the northeast Tibetan plateau, which is marked by red rectangle in the inset map, **b** is marked by a blue rectangle and main faults are represented by black dashed lines. **b** Regional geologic structures around Gonghe Basin (modified from (Zhao et al. 2020)). Abbreviations: Kunlun Fault (KLF), North China Suture (NCS), Altyn Tagh Fault (AFT), Ainimaqing Auture Zone (ANMQ), Qinghai Nan Shan Fault (QHNFS), Duohemao Fault (DHMF), Elashan Fault (ELSF), Shagou Fault (SGF), Xinjie Fault (XJF), Wayuxiang Fault (WY-GNF), Gonghe Nan Shan Fault (GHNSF), Moganshan Fault (MGF). AA 'and BB' are two seismic survey lines, respectively, from (Jia et al. 2019) and (Zhang et al. 2011)

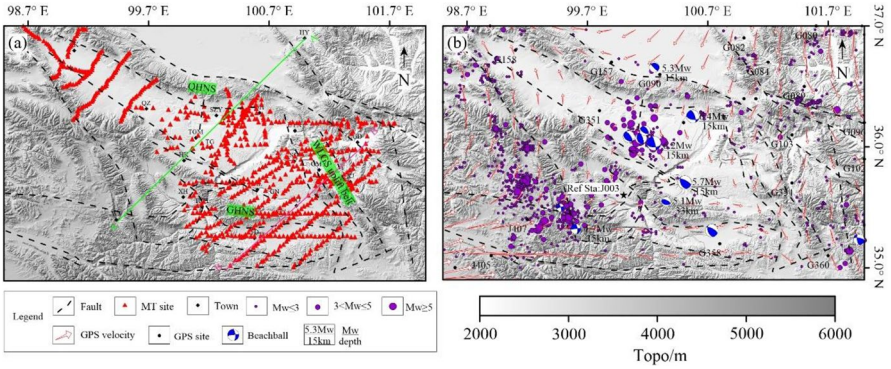

Fig. 2 Distribution map of GPS sites, earthquake and magnetotelluric survey points. **a** Distribution of magnetotelluric survey points and earthquake events (1950–2021) around the study area. Earthquake events are represented by white dots of different sizes according to magnitude. The earthquakes indicated by purple dots are obtained from China Earthquake Administration catalog (downloaded from http://www.ceic.ac.cn/), and beach balls represent focal mechanisms (downloaded from http://www.globalcmt.org). **b** GPS displacement field in and around Gonghe Basin (with J003 GPS station as reference) and focal mechanism solution of main earthquake events. The black dotted line is the fault, and the blue and white beach ball is the focal mechanism solution. AA 'and BB' are the same as Fig. 1. Abbreviation: Qinghai Nanshan Mount (QHNS), Gonghe Nanshan Mount (GHNS)

observation station J003, located close to GHNS as the reference point to plot the velocity field of Gonghe Basin and other GPS stations around it (Fig. 2b). Overall, with J003 as the center, the velocity vector converges to the basin from southwest to northeast. Near QHNS and GHNS, the velocity vector converges in northeast and southwest directions, with the direction of velocity vector is consistent with the direction of primary faults in the area. The GPS velocity field results provide an intuitive picture of the current tectonic deformation mode of SN shortening and EW extension deformation of Tibetan Plateau. Deep dynamic causes of surface displacement and deformation, from the outside to the inside, are worthy of further study. To better understand the mechanism of tectonic deformation, we deployed a magnetotelluric survey covering the entire basin (Fig. 2a).

Observation and data processing

The broadband magnetotelluric survey was completed by the Geophysical and Geochemical Exploration Institute of the Chinese Academy of Geological Sciences, the Hydrological Environment and Geological Environment Survey Center of the Chinese Academy of Geological Sciences, and the Chinese Academy of Geological Sciences in 2018–2021. In total, 710 survey points were studied using the Crystal Global Aether (https://www.crystalglobegeo.com/) Instrument and Phoenix MTU-5A (http://www.phoenix-geophysics.com) instrument. At each measuring point, two horizontal electric field components (Ex, Ey) and three magnetic field components (Hx, Hy, Hz) were recorded over a time series of 20 h.

Data collected by MTU-5A and Aether were processed using prMT software (https://www.crystalglobegeo.com/). The collected magnetotelluric time series was converted to the frequency domain using standard robust algorithms (Egbert and Booker 1986) and remote reference technology (Gamble et al. 1979). This allowed us to obtain impedance

tensors and select the power spectrum for improved results during processing using interactive methods. We then used MT Pioneer software (Chen et al. 2004b) to eliminate high noise impedance tensors. Upon completion of the data standardization process, we performed logarithmic interval resampling on all data, eventually obtaining the response values of 59 frequency points within the frequency range of 320 Hz to 0.000461936 Hz.

To avoid electrical distortion caused by near-surface non-uniformity, we employed the phase tensor decomposition technique proposed by Ref. (Caldwell et al. 2004). We used different periods at each station in the basin to color the phase tensor ellipses β (Fig. 3). At 80 Hz, the absolute values of the slope angle of most phase tensor ellipses are less than 3, indicating that the shallow resistivity structure is more likely to be 1D or 2D. During the 1 s period, β in the basin is small, and the ellipse show no obvious directionality. However, in the vicinity of the basin–mountain transition zone and in the mountainous regions, the β is significantly large, and the ellipse demonstrate clear directionality, This suggests that these areas have a relatively more complex structure. β associated with periods greater than 100 s exhibit an overall slope value exceeding 3, and tensor ellipses exhibit varied directions, implying increased complexity. Oblique analysis indicates that the structure at the junction of the Gonghe Basin and the middle-to-deep parts of the basin are likely three-dimensional. Therefore, 3D magnetotelluric sounding inversion should be carried out in the Gonghe Basin.

3D Magnetotelluric inversion

We used the ModEM software package (Egbert and Kelbert 2012; Kelbert et al. 2014) to invert the collected magnetotelluric data. When inverting, a 1.5 km by 1.5 km grid is used in the horizontal direction, with six external expansion grids, 1.5 external expansion factors,

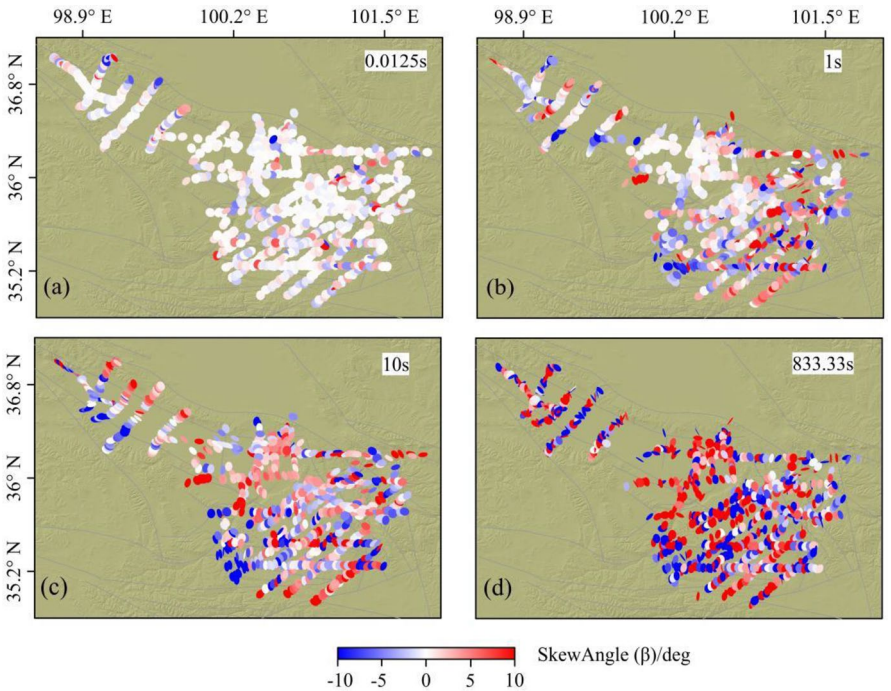

Fig. 3 Skew values for different periods at each measurement point

and 169 × 202 horizontal grids. The first layer depth in the vertical direction is 25 m, with a layer thickness increasing factor of 1.11. Five external expansion grids, 1.5 external expansion factors, and 60 external expansion grids we used. The bottom grid node is located at 609.56 km. Due to the lack of prior information, we used a uniform half space as the initial model (Hill et al. 2015). We used a uniform half space resistivity model (50 Ω. m, 100 Ω. m, and 500 Ω. m, respectively) for trial calculations. Ultimately, a uniform half space of 100 Ω.m was chosen as the initial model to invert the obtained resistivity structure as the explanatory model, based on geological data and fitting difference distribution.

To improve the vertical resolution, we selected 59 frequencies within the range of 320 Hz–0.000461936 Hz as the inversion period for the final resistivity model. In the inversion, a 5% error lower limit was set for the Zxy and Zyx impedance components. After 113 iterations, the RMS decreased from 11.376 to 1.033. Figure 4 shows the fitting error of the impedance tensor at each measurement point, with the vast majority of points having a fitting error below 3%, indicating a good fit. A comparison of the measured data at a frequency of 0.56 Hz with the inversion fitting data (Fig. 5) shows a good match of the inversion resistivity and phase at each measurement point at 0.56 Hz with the observed resistivity and phase, indicating that the overall inversion results are satisfactory.

To verify the reliability of high conductivity anomaly and high resistivity anomaly in three-dimensional inversion resistivity model, we use a resistivity of 100 Ω.m to replaces the resistivity of the three abnormal blocks at four depths to understand how model changes affect the final data fitting (Fig. 6). We used the parameter RMS_{Update} (%) to check how the data fit changes, which is defined as follows (Garcia et al. 2015; Ye et al. 2018a):

$$RMS_{Update} = \frac{RMS_0 - RMS_1}{RMS_0} \times 100\%,$$

where RMS_0 is the RMS misfit value for the original preferred inversion model and RMS_1 is that for the test model. By definition, a negative RMS_{Update} value indicates a deterioration data fitting compared to the original preferred model, whereas a positive RMS_{Update} value suggests a better data fitting.

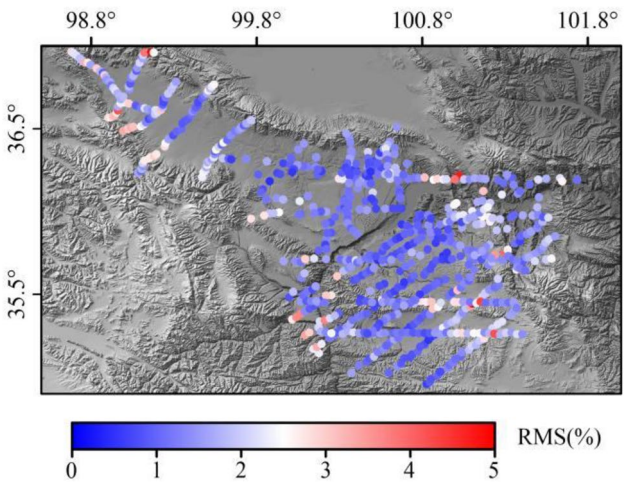

Fig. 4 3D inversion fitting error

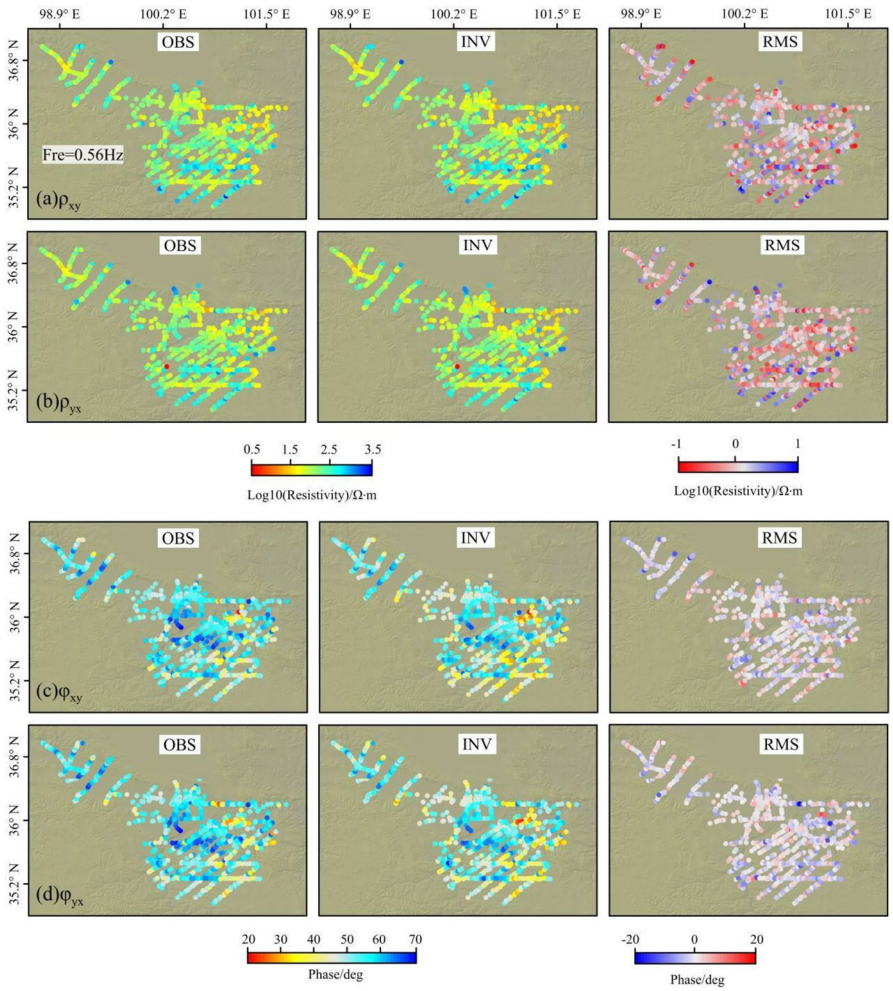

Fig. 5 Observations, fit values, and residuals of each measurement point at 0.56 Hz. **a** Resistivity of xy, **b** resistivity of yx, **c** phase of xy, **d** phase of yx

Figure 6 shows the RMS_{Update} values of MT measuring points in four sensitivity tests. The model employed in three-dimensional inversion is to resets the resistivity blocks in four depth ranges to 100 Ω. m, respectively. These four depths are continuous on the initial model grid of 3D inversion, and their depth range is consistent with the initial inversion network. Figure 6a–c shows the RMS_{Update} of most measuring points is negative and significantly increases (> 5%), indicating that the data fitting is worse. However, the RMS_{Update} of most measuring points in Fig. 6d is small and close to 0, suggesting that the data fitting is not sensitive to the test model. Figure 6c illustrates that the test model at the depth of 36.72 km fails to fit the observation data well, while Fig. 6d shows that the observation data are not sensitive to the test model at the depth of 42.74 km. Therefore, we conclude that the three-dimensional resistivity model shown in Fig. 6 is reliable at a depth of about 35 km.

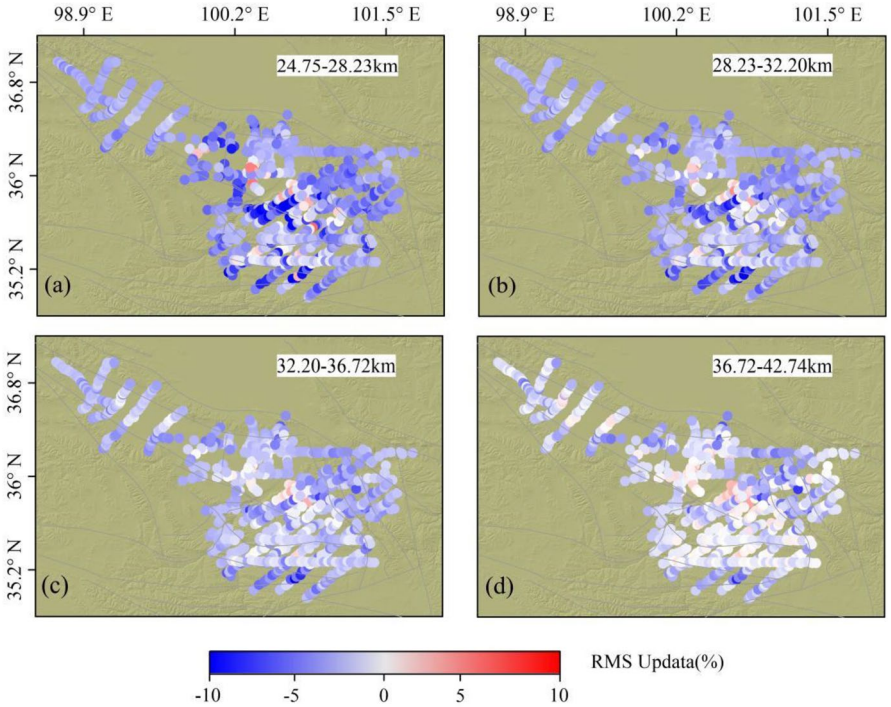

Fig. 6 RMS_{Update} of each magnetotelluric sounding station. **a**, **b**, **c**, **d**, respectively, represents the RMS_{Update} value obtained by replacing the four adjacent layers of 24.75–28.23 km, 28.23–32.20 km, 32.20–36.72 km and 36.72–42.74 km in the resistivity model obtained by inversion with 100 Ω resistivity value in each station

Interpretation and discussion

From the three-dimensional inversion resistivity slice (Fig. 7a–c), we can clearly see the structural framework of Gonghe basin. The high conductivity corresponds to the depression in Gonghe Basin (light blue and yellow). Due to the existence of loose sedimentary layers, the resistivity in the basin is relatively low, whereas the mountains surrounding the basin are electrically high. Notably, WLGSZ divides the basin into east and west parts (Zhang et al. 2018b).

Electrical structural characteristics of the Gonghe Basin

The resistivity at the basin mountain junction changes sharply, and the inferred fault①-⑥ (Fig. 7e) has a good corresponding relationship with the surface fault (Fig. 1b). The WLGSZ is generally characterized by high resistivity, extending from the shallow surface to the middle and lower crust (Fig. 7b–e). Its western side is controlled by the thrust strike-slip fault SGF and its east side is XJF. In the north, QHNSF is distributed in NWW direction defining the northern boundary of the basin. The fault was formed in Mesozoic era, and there is still strong activity in the Cenozoic era. A magnitude 6.4 earthquake occurred in 1990 (Figs. 2b and 9b). WY-GNF fault is a NW trending thrust strike slip fault, which is still active in the Holocene (Zheng 1999) and has triggered many earthquakes (Figs. 2b and 9b, c). In fact, after projecting the earthquake locations onto the resistivity profile, we found that earthquakes often occur near the contact zone of high and low resistivity blocks (Fig. 9a, b, c). There is a coupling relationship

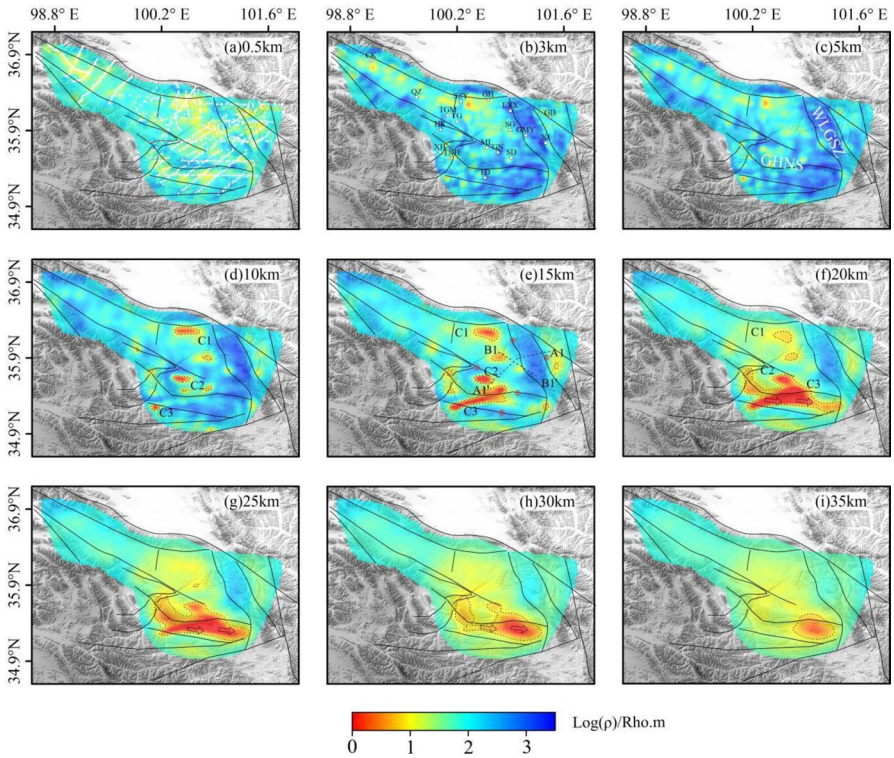

Fig. 7 Horizontal slices of the 3D resistivity model for different depths: **a** 0.5 km, **b** 3 km, **c** 5 km, **d** 10 km, **e** 15 km, **f** 20 km, **g** 25 km, **h** 30 km, **i** 35 km. The RMS misfit of the 3D resistivity model is 1.03, and the number of iterations is 86. The white triangles in **a** represent magnetotelluric stations. The black solid lines depict active faults (Wang et al. 2017). The faults ①–⑥ are the same as those in Fig. 1b. C1–C3 represent the three conductive anomalous. Townships labeled in **b** include CK, Chaka; GD, Guide; SZY, Shazuyu; GH, Gonghe; HK Heka; XH, Xinghai; ML, Mangla; GN, Guinan and TD, Tongde. The magnetotelluric Profiles A1A1′ and B1B1′ in Ref. (Gao et al. 2020) is shown by the black dashed line in **e**. The solid arrows shown in **f**–**h** indicate the possible direction of the lower crustal channel flow, inferred from this study. WLGSZ labeled in **c** instead of Waliguanshan uplift belt, GHNS instead of Gonghenanshan

between low resistivity and faults. These low resistivity zones may act as detachment surfaces during geological movement. When stress is released, the geological body slides along the fault, and earthquakes occur. Significant high-conductivity bodies (resistivity less than 10 Ω. m) are marked with C1, C2 and C3, respectively, on Fig. 7. The resistivity distribution obtained in this works is similar to Gao's results (Gao et al. 2020), but the high-conductivity scale we obtained along B1B1′ is smaller and the resistivity value is higher than Gao. As the depth increase, C3 extends significantly to the east, C2 tilts to the southeast, and is connected with C3 in depth, and continuously distributed at a depth of 15-35 km (Figs. 7e–i and 8b). This corresponds to the results of seismic tomography in this area. On the profile of the western Qinling orogenic belt along the Songpan block, there is a continuous P-wave and S-wave low-velocity layer from west to east at a depth of 15–40 km (Xiao and Gao 2017; Xia et al. 2021). Meanwhile, we note that this high conductivity is connected with the high conductivity strip C1 at the north end of the basin in the deep, indicating that the deep high conductivity material which exists in the front of the mountain and becomes the heat source in the crust, may be extruded to the north and blocked by QHNS. This understanding is consistent with the magnetotelluric survey results carried out by Ref. (Gao et al. 2018) in the basin. Correspondingly,

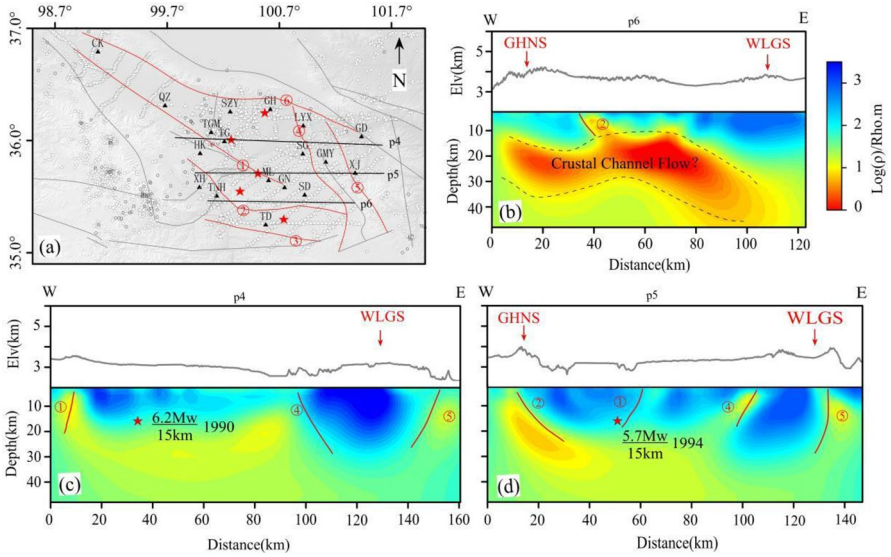

Fig. 8 Vertical slices of different sections along the EW direction. **a** E–W sections location. The black and red solid lines depict active faults (Wang et al. 2017). The faults ①–⑥ are the same as those in Fig. 1b. Red stars represent major earthquakes, and black rectangles represent the same place names as Fig. 7b. **b** Profile p6, **c** Profile p4, **d** Profile p5

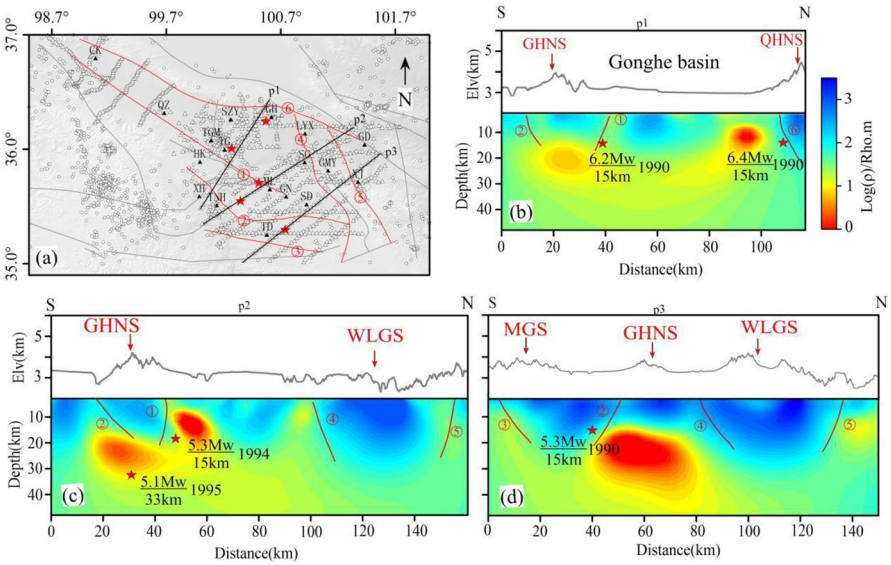

Fig. 9 Vertical slices of different sections along the NE direction. **a** NE sections location. The black and red solid lines depict active faults (Wang et al. 2017). The faults ①–⑥ are the same as those in Fig. 1b. Red stars represent major earthquakes, and black rectangles represent the same place names as Fig. 7b. **b** Profile p6, **c** Profile p4, **d** Profile p5

there is recognition that there is a low-speed layer under the Gonghe Basin in the seismic tomography of the section along the Songpan block to the Qilian orogenic belt (Xia et al. 2021), and the thickness of this low-speed layer gradually narrows from south to north and significantly thins before QHNS (Fig. 10a). This indicates that the deep crustal material of the Tibetan Plateau moves weakly from south to north and may be blocked

by QHNS. The results of Ref. (Jia et al. 2019) also confirmed that there is a low-velocity layer extending northward in the crust and the middle crust beneath the Gonghe Basin is missing (Fig. 10a).

In contrast, the WLGSZ shows high resistivity overall in the resistivity slice (Fig. 6b–i), and extends to the middle and lower crust (30 km) in the vertical direction (Figs. 8 and 9), which is mainly reflected in the blocking of the eastward movement of materials in the middle and upper crust, so that the eastward materials may flow deeper into the West Qinling structural belt. The existence of low velocity and high-conductivity layers indicates that granitization, melting and regional metamorphism are taking place in this area (Feldman 1976). Many geotectonists believe that the low-velocity layer in the crust is the detachment surface in the crust, while petrologists believe that it is the source

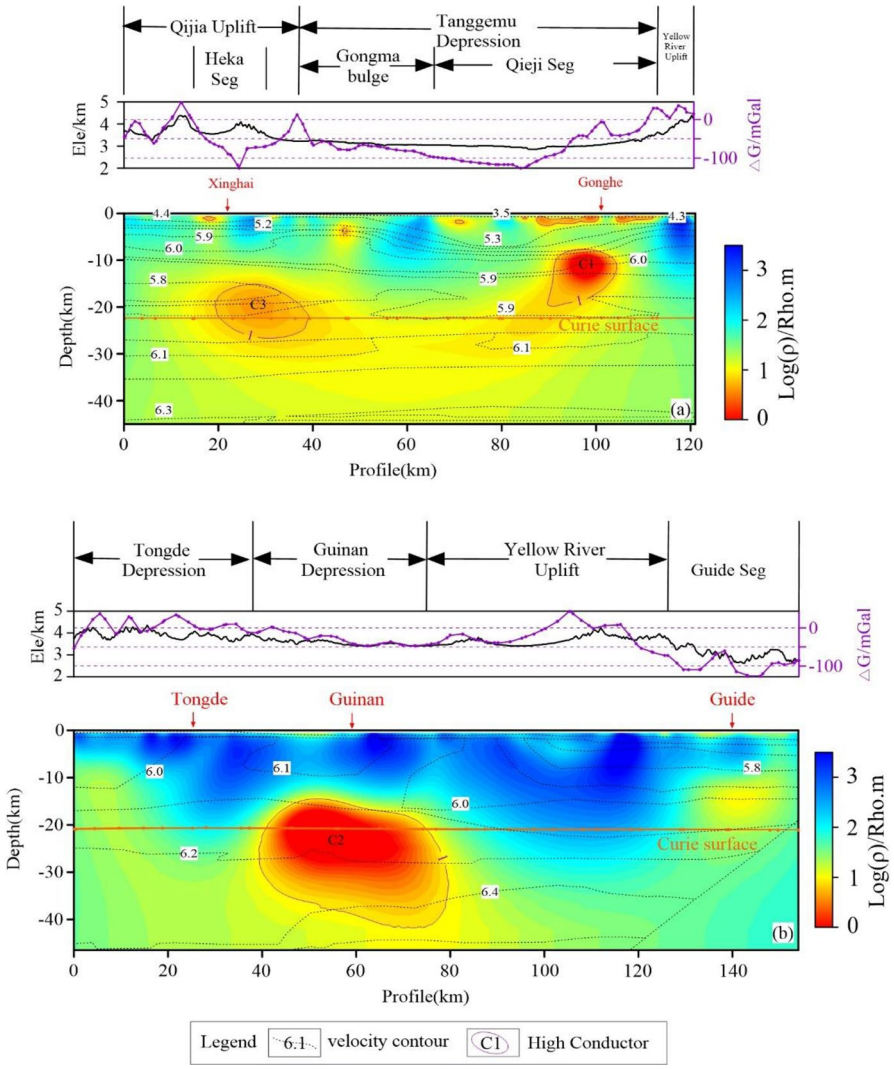

Fig. 10 Comprehensive profile of resistivity, seismic wave velocity (Vp) and gravity anomaly. **a** Section p1, **b** Section p3. The positions of p1 and p3 are consistent with Fig. 9a. The elevation is derived from DEM data. Gravity anomaly data are from Ref. (Hirt et al. 2013). Seismic wave velocity (Vp) AA 'comes from Ref. (Jia et al. 2019), and BB' comes from Ref. (Zhang et al. 2011), their positions are shown in Fig. 2a. The Curie depth data are from Ref. (Zhao et al. 2020)

of granitic magma. In fact, the two are likely to be both (Feng et al. 2002). Although the geophysical sections northward (along the Songpan Qilian direction) and eastward (along the Songpan Qinling direction) on the northeastern margin of Tibetan Plateau show that there are low-speed and high-conductivity layers in the crust, the deformation and uplift modes in deep may be differences (Clark and Royden 2000; Ye et al. 2018a) proposed a lower Crustal Channel Flow model to explain the topographic changes in the eastern part of the Tibetan Plateau. Many geophysical investigations have found that the lower crustal flow of the southeast branch squeezed into the Sichuan-Yunnan and Indo-Chinese blocks in the form of channels and achieved good results (Liu et al. 2014; Bai et al. 2010; Bao et al. 2015). The Qinling Mountains may be used as an extrusion channel for the flow of the other branch to the northeast. This study shows that the northward direction of the Gonghe Basin is mainly controlled by deformation and uplift in the crust, and there may be material flow in the crust in the eastward direction (Qinling Mountains) (Fig. 1a).

Comprehensive geophysical profile characteristics

To more accurately describe the state of underground media, especially the thermal state, which may be closely related to the high geothermal flow values in the Gonghe Basin, we superimpose the seismic wave velocity profile onto the resistivity profile (p1/p3 is the same as the position in Fig. 9). This is done in combination with the gravity anomaly to analyze the underground state of matter.

The electrical profile in Fig. 10a shows that the middle and shallow parts of the Qieji Sag and Guide Sag have low resistivity, which is corresponds to the thicker Cenozoic loose sediments in the sag. The seismic wave velocity is also low. The low value of gravity anomaly further indicates its low density. In contrast, the Qijia uplift and the Yellow River uplift show high resistivity in the middle and shallow parts, which corresponds to the Mesozoic strata and magmatic facies. The seismic waves velocities here are high, and gravity anomaly also shows high values, indicating a medium relatively high density causing gravity anomaly. We have delineated the high conductor on the profile using a resistivity threshold of 10 ohms. Shallow high conductors are generally believed to be related to Cenozoic sedimentation, while mid-deep low resistivity bodies may be related to partial melting of the crust (Bai et al. 2010; Gao et al. 2018, 2020). Both resistivity profiles indicate the presence of high-conductivity anomalous bodies deep within the basin, represented by C1, C2, and C3, respectively. At depth, these high conductors are distributed within a range of 15–35 km underground. Their centers align with the Curie surface, indicating that demagnetization occurred in the underground medium at this depth due to high temperature (Xiong et al. 2014). The longitudinal wave of seismic wave shows a noticeable low-velocity layer along the northeast direction of the Gonghe Basin, with the wave velocity decreases from 6.0 km/s to 5.9 km/s. Below Xinghai (Fig. 10a), the wave velocity is even dips 5.8 km/s, potentially related to the northward and eastward crustal material flow of the Tibetan Plateau (Ye et al. 2018b). Correspondingly, there is a gap below the Gonghe Basin in the seismic wave velocity surface, indicating a missing lower boundary of the upper crust (Jia et al. 2019). Partial melting and fluid flow often cause low wave velocity anomalies (McKenzie et al. 2005; Priestley and Kenzie 2006),

where the P-wave velocity decreases by 0.5% to 2% for every 100 ℃ increase in temperature (Goes et al. 2000).

Estimation of melting volume of high conductors in the middle and lower crust

The comprehensive geophysical exploration results show that there are low-speed, high-conductivity and low-density materials under the Gonghe Basin. The geophysical information observed on the surface is closely related to the deep material migration, crustal lithosphere deformation and deep dynamic process state (Lü et al. 2022). Rock conductivity experiment shows that the main factors influencing the conductivity of deep crustal rocks are temperature and pressure. When the rock nears melting temperature, the conductivity will be several orders of magnitude higher than at room temperature (Ma et al. 2005), causing dry rocks in the crust and upper mantle becoming more conductive. The electrical structural characteristics of the crust and mantle largely depend on the underground thermal state (Wei et al. 2006). Temperature is the main external factor affecting the conductivity of minerals and rocks (Jones et al. 2009), and the relationship between conductivity and temperature follows Arrhenius' law, expressed as:

$$\sigma = \sigma_0 \exp\left[\left(\frac{-E_a + P \times \Delta V}{RT}\right)\right].$$

In this formula, σ is rock conductivity (S/m), σ_0 is conductivity pre-exponential factor (S/m), E_a is activation energy (J), P is pressure (MPa), $-E_a + P \times \Delta V$ represents activation volume. R is the gas constant (8.314 J/k), and T is absolute temperature (K). Concerning the fitting coefficient of the formula, Ref. (Guo et al. 2018) rewritten the Arrhenius empirical formula based on the parameters obtained from granite high-temperature and high-pressure tests as follows:

$$\log\sigma = 3.205(\pm 0.067) - 0.102(\pm 0.016)w - \frac{4228.5((\pm 83.2) - 354.7(\pm 18.1)w + 693.6(\pm 37.8)P}{T}.$$

In this formula, σ represents electrical conductivity in S/m, T stands temperature in K, P denotes pressure in GPa, and *w* is H2O content in *wt* %. According to the formula, conductivity increases with a rise in both water content and temperature, and these two physical quantities have the most significant influence (Fig. 11a). Moreover, the variation in conductivity is closely linked to the melting volume of underground media. We have used Hashin Shtrikman upper bound (Paul et al. 2000) to constrain conductivity and the volume of melting. The expression is as follows:

$$\sigma_{eff+} = \sigma_2\left(1 - \frac{3(1-\gamma_2)(\sigma_2 - \sigma_1)}{3\sigma_{2-}\gamma_2(\sigma_2 - \sigma_1)}\right),$$

where σ_{eff+} represents the effective conductivity of the rock mass with the volume fraction of the melt, σ_2 and σ_1 are the conductivities of the host rock mass and molten rock mass, respectively, and γ_2 is the melt volume fraction.

We used the three high conductors in Fig. 10 to estimate the melting volume. C3, a high conductor, is situated on the southern side of the Gonghe Basin near the Kunlun Fault and is notably representativeness. We used the recorded temperature of 209 ℃ at the bottom of the GH01 hole 4000 m (Zhang et al. 2021) as a reference for temperature

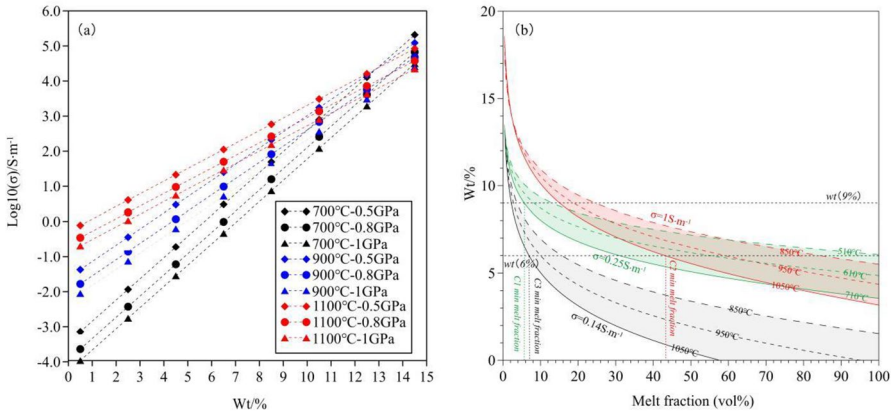

Fig. 11 Temperature, pressure, and conductivity relationship curve. **a** The relationship between conductivity and water content under different temperature and pressure conditions. **b** The relationship between water content, melting percentage, and conductivity

constraints, calculating linearly. Hence, the medium's temperature at a depth of 15 km is approximately 750 ℃, and the temperature at a depth of 20 km is about 1050 ℃.

From Fig. 10's cross-section, we deduced that the average conductivity of C3 is about 1S/m, and the background conductivity is 0.0005S/m. We considered a temperature range of 850 ℃–1050 ℃, with a pressure of about 1Gpa, and a water content of about 6–9% (Guo et al. 2018). We calculated the changes in resistivity under these constraints of water content and temperature. Given the typical H2O contents in crustal magma and the applicable range of our electrical conductivity model, we set the upper limit of H_2O content of granitic melt was set at 9 wt %. From Fig. 10, we noted the average conductivity of C2 is approximately 0.14S/m, with the background conductivity is 0.0005S/m. C2 and C3 have similar depths, so we applied the same temperature and pressure conditions are taken. The temperature and pressure of C1 are references from C3 but decrease with depth, with pressure at 0.6 Gb and a temperature range of 550 ℃–750 ℃. The average conductivity of C1 is approximately 0.25S/m, and the background conductivity is 0.0025S/m.

Figure 11 reveals that the melting volume of C3 high conductor varies between 3 and 16% within the water content constraint range. This is slightly lower than the melting volume of other high conductors obtained under the Songpan Ganzi block by magnetotelluric methods (4–21%) (Wang et al. 2016b; Unsworth et al. 2005; Wei et al. 2014). The melting volume of C2 high conductor varies greatly, about 15%–86%. The melting volume of C1 is about 6%–99%. In fact, the C2 and C3 has an approximate burial depth, so the temperature and pressure conditions and water content should be similar. If the temperature and pressure conditions remain unchanged and the highest temperature is 1050 ℃, the melting volume of C3 is about 7%, and the melting volume of C2 is about 43%. This suggests that the C2 high conductor in the southeast of the basin may have more "fluidity", while the relative C3 exhibits "plasticity". Due to its shallow burial depth, C1's high conductivity may be more related to an increase in water content. Therefore, considering the constraints of higher water content and temperature, its melting volume is about 6%, similar to Ref. (Zhang et al. 2021)'s estimation of 4% to 7% of the melting volume in the western part of the Gonghe Basin.

The resistivity of underground media obtained by the magnetotelluric method in the Gonghe basin is determined by several factors, with temperature and water content are the decisive factors. Melt bodies are commonly present in the middle and lower crust of the Gonghe Basin. These melt bodies serve as ductile sliding layers, providing detachment for crustal shortening and deformation in the northeastern margin of the Tibetan Plateau. Additionally, they act as natural heat sources transmitting heat to the basin's upper part, contributing to the current high geothermal background pattern of the Gonghe basin.

Conclusions

Through three-dimensional imaging of magnetotelluric data from 710 measurement points, we obtained a three-dimensional resistivity model for the entire Gonghe basin and the southeastern region. This region is situated in the compression deformation zone of the northeastern edge of the Tibetan Plateau, possessing rich geothermal resources. The study holds substantial significance for understanding the deformation, uplift mechanism of the northeastern part of the Tibetan Plateau, and its impact geothermal resource. The 3D inversion resistivity model reveals that high conductivity bodies are widely distributed in the middle and deep parts of the Gonghe Basin. These bodies are characterized by low wave velocity and low gravity anomaly when compared through cross-sections. Based on high-temperature and high-pressure rock test results, it is estimated that these high conductors likely have high temperatures and undergo partial melting (3–43%). This phenomenon is a crucial factor contributing to the current high geothermal background in the Gonghe basin as supported by multiple high-temperature dry hot rock boreholes such as GR1 and GH01. Additionally, we conducted resistivity imaging of faults associated with surface topography changes in the Gonghe basin. The findings showed that these faults played a significant role in the formation of GHNS, WLGS, and QHNS during the expansion of the Tibetan Plateau towards the northeast edge. At deep, these faults are connected to a high conductor in the middle and upper crust, which can serve as a detachment layer for crustal shortening and deformation. They also act as a heat source, transmitting heat upwards.

Acknowledgements
We thank Gary Egbert and Anna Kelbert for providing the ModEM package. The three-dimensional magnetotelluric inversion in this research work were performed on the Geological Cloud Platform of CGS.

Author contributions
Conceptualization, YY and XW; data curation, YY, JZ and ML; formal analysis, YY; funding acquisition, YY, JZ, DJ and ML; investigation, YY, XL and XT; methodology, YY, XW. and ML; software, YY and ML; validation, YY, LM and DJ; visualization, YY, ZZ, LM and YO; writing—original draft, YY; writing—review and editing, YY, ZZ and XW. All authors have read and agreed to the published version of the manuscript.

Funding
This research was funded by Basic Scientific Research Funds Project of Chinese Academy of Geological Sciences (JKYQN202350; JKYZD202330) and Geological survey Project of China Geological Survey (grant number DD20201105; DD20221639; DD20230548).

Availability of data and materials
Data associated with this research are available and can be obtained by contacting the corresponding author.

Declarations

Competing interests
The authors declare that they have no competing financial interests.

Received: 5 July 2023 Accepted: 2 January 2024
Published online: 15 February 2024

References

Abdelfettah Y, Sailhac P, Larnier H, Matthey PD, Schill E. Continuous and time-lapse magnetotelluric monitoring of low volume injection at Rittershoffen geothermal project, northern Alsace—France. Geothermics. 2018;71(B2):1–11. https://doi.org/10.1016/j.geothermics.2017.08.004.

Amatyakula P, Boonchaisukb S, Rung-Arunwanc T, Vachiratienchaic C, Spencer HW, Piraraie K, Fuangswasdie A, Siripunvaraporn W. Exploring the shallow geothermal fluid reservoir of Fang geothermal system, Thailand via a 3-D magnetotelluric survey. Geothermics. 2016;64:516–26. https://doi.org/10.1016/j.geothermics.2016.08.003.

Bai DH, Unsworth MJ, Meju MA, Ma XB, Teng JW, Kong XR, Sun Y, Sun J, Wang LF, Jiang CS, Zhao CP, Xiao PF, Liu M. Crustal deformation of the eastern Tibetan Plateau revealed by magnetotelluric imaging. Nat Geosci. 2010;3:358–62.

Bao XW, Sun XX, Xu MJ, Eaton WD, Song XD, Ding ZF, Mi N, Li H, Yu DY, Huang ZC, Wang P. Two crustal low-velocity channels beneath SE Tibet revealed by joint inversion of Rayleigh wave dispersion and receiver functions. Earth Planet Sci Lett. 2015;415:16–24. https://doi.org/10.1016/j.epsl.2015.01.020.

Caldwell TG, Bibby HM, Brown C. The magnetotelluric phase tensor. Geophys J Int. 2004;158:457–69. https://doi.org/10.1111/j.1365-246X.2004.02281.x.

Chen QZ, Freymueller JT, Yang ZQ, Xu CJ, Jiang WP, Wang Q, Liu JN. A deforming block model for the present-day tectonics of Tibet. Jgeophys Res. 2004a;109:B01403. https://doi.org/10.1029/2002JB002350.

Chen XB, Zhao GZ, Zhan Y. A visual integrated windows system for MT data process and interpretation. Oil Geophys Prospect. 2004b;39:11–6.

Cheng YZ, Pang ZH, Kong YL, Chen XB, Wang GJ. Imaging the heat source of the Kangding high-temperature geothermal system on the Xianshuihe fault by magnetotelluric survey. Geothermics. 2022;102:102386. https://doi.org/10.1016/j.geothermics.2022.102386.

Clark MK, Royden LH. Topographic ooze: building the eastern margin of Tibet by lower crustal flow. Geology. 2000;28:703–6. https://doi.org/10.1130/0091-7613.

Craddock WH, Kirby E, Zhang H, Clark MK, Champagnac JD, Yuan D. Rates and style of Cenozoic deformation around the Gonghe Basin, northeastern Tibetan Plateau. Geosphere. 2014;10:1255–82. https://doi.org/10.1130/GES01024.1.

Darnet M. On the origins of self-potential (SP) anomalies induced by water injections into geothermal reservoirs. Geophys Res Lett. 2004;31(19):226. https://doi.org/10.1016/j.geothermics.2017.08.004.

Darnet M, Wawrzyniak P, Coppo N, Nielsson S, Schill E, Fridleifsson GÓ. Monitoring geothermal reservoir developments with the controlled-source electro-magnetic method—a calibration study on the Reykjanes geothermal field. J Volcanol Geotherm Res. 2020;391:106437. https://doi.org/10.1016/j.jvolgeores.2018.08.015.

Dewey JF, Burke CA. Tibetan, Variscan, and Precambrian basement reactivation:products of continental collision. J Geol. 1973;81:683–92. https://doi.org/10.1086/627920.

Egbert GD, Booker JR. Robust estimation of geomagnetic transfer functions. Geophys J R Astron Soc. 1986;87:173–94. https://doi.org/10.1111/j.1365-246X.

Egbert GD, Kelbert A. Computational recipes for electromagnetic inverse problems. Geophys J Int. 2012;189:251–67. https://doi.org/10.1111/j.1365-246X.2011.05347.x.

Feldman IS. On the nature of conductive layers in the earth's crust and upper mantle. Geoelectr Geotherm Stud. 1976;1:721–30.

Feng YM, Chao XD, Zhang EP, Hu YX, Pan XP, Yang JL, Jia QZ, Li WM. Structure, orogenic process and dynamics of the West Qinling orogenic belt. Xi'an: Xi'an Map Press; 2002.

Flores C, Esquivel TA, Galván CA, Salas JL. Seal cap resistivity structure of Los Humeros geothermal field from direct current and transient electromagnetic soundings. Geofísi Int. 2022;61(4):351–76. https://doi.org/10.22201/igeof.00167169p.2022.61.4.2228.

Gamble TD, Goubau WM, Clarke J. Magnetotellurics with a remote magnetic reference. Geophysics. 1979;44:53–68.

Gao J, Zhang HJ, Zhang SQ, Chen XB, Cheng ZP, Jia XF, Li ST, Fu L, Gao L, Xin HL. Three-dimensional magnetotelluric imaging of the geothermal system beneath the Gonghe Basin Northeast Tibetan plateau. Geothermics. 2018;76:15–25. https://doi.org/10.1016/j.geothermics.2018.06.009.

Gao J, Zhang HJ, Zhang HP, Zhang SQ, Cheng ZP. Three-dimensional magnetotelluric imaging of the SE Gonghe Basin: Implication for the orogenic uplift in the northeastern margin of the Tibetan Plateau. Tectonophysics. 2020;789:228525. https://doi.org/10.1016/j.tecto.2020.228525.

Garcia X, Seillé H, Elsenbeck J, Evans RL, Jegen M, Lovatini A, Martí A, Marcuello A, Queralt P, Ranero CR, Ungarelli C. Structure of the mantle beneath the Alboran Basin from magnetotelluric soundings. Geochem Geophys Geosyst. 2015;16:4261–74. https://doi.org/10.1002/2015GC006100.

Goes S, Govers R, Vacher P. Shallow mantle temperatures under Europe from P and S wave tomography. J Geophys Res Solid Earth. 2000;105:11153–69. https://doi.org/10.1029/1999jb900300.

Guo B, Liu QY, Chen JH, Zhao DP, Li SC, Lai YG. Seismic Tomographic imaging of the crust and upper mantle beneath the northeastern edge of the Qinghai-Xizang Plateau and the Ordos Area. Chin J Geophys. 2004;5:790–197. https://doi.org/10.3321/j.issn:0001-5733.2004.05.009.

Guo X, Zhang L, Su X, Mao Z, Gao XY, Yang X, Ni H. Melting inside the Tibetan crust? Constraint from electrical conductivity of peraluminous granitic melt. Geophys Res Lett. 2018;45:3906–13. https://doi.org/10.1029/2018GL077804.

Hashimoto T, Kanda W, Morita Y, Hayakawa M, Tanaka R, Aoyama H, Uyeshima M. Significance of electromagnetic surveys at active volcanoes: toward evaluating the imminence of wet eruptions. J Disaster Res. 2019;14(4):580–91. https://doi.org/10.20965/jdr.2019.p0580.

He BZ, Zheng ML, Yun XR, Cai ZH, Jiao CL, Chen XJ, Zheng Y, Ma XX, Liu LH, Chen HM, Zhang SS, Lei M, Fu GQ, Li ZY. Structural architecture and energy resource potential of Gonghe Basin NE Qinghai-Tibet Plateau. Earth Sci Front. 2023;30:81–105. https://doi.org/10.13745/j.esf.sf.2022.8.35.
Hill GJ, Bibby HM, Ogawa Y, Wallin EL, Heise W. Structure of the Tongariro Volcanic system: insights from magnetotelluric imaging. Earth Planet Sci Lett. 2015;432:115–25. https://doi.org/10.1016/j.epsl.2015.10.003.
Hirt C, Claessens SJ, Fecher T, Kuhn M, Pail R, Rexer M. New ultra-high resolution picture of Earth's gravity field. Geophys Res Lett. 2013;40:4279–83. https://doi.org/10.1002/grl.50838.
Jia SX, Guo WB, Mooney WD, Wang FY, Duan YH, Zhao JM, Lin JY, Liu Z. Crustal structure of the middle segment of the Qilian fold belt and the coupling mechanism of its associated basin and range system. Tectonophysics. 2019;770:1–14. https://doi.org/10.1016/j.tecto.2019.06.024.
Jones AG, Evans RL, Eaton DW. Velocity-conductivity relationships for mantle mineral assemblages in Archean cratonic lithosphere based on a review of laboratory data and Hashin Shtrikman extremal bounds. Lithos. 2009;109:131–43. https://doi.org/10.1016/j.lithos.2008.10.014.
Kelbert A, Meqbel N, Egbert GD, Tandon K. ModEM: a modular system for inversion of electromagnetic geophysical data. Comput Geosci. 2014;6:40–53. https://doi.org/10.1016/j.cageo.2014.01.010.
Li HB, Pan JW, Sun ZM, Si JL, Pei JL, Liu DL, Marie LC, Wang H, Lu HJ, Zheng Y, Li CR. Continental tectonic deformation and seismic activity: a case study from the Tibetan Plateau. Acta Geol Sin. 2021;95:194–213. https://doi.org/10.19762/j.cnki.dizhixuebao.2021051.
Liu QY, Der Hilst RD, Li Y, Yao HJ, Chen JH, Guo B, Qi SH, Wang J, Huang H, Li SC. Eastward expansion of the Tibetan plateau by crustal flow and strain partitioning across faults. Nat Geosci. 2014;7:361–5. https://doi.org/10.1038/ngeo2130.
Lü JY, Shen XZ, Jin RZ, Huang LT. Laterally heterogeneous crustal anisotropy in the northeastern margin of Tibetan Plateau and its tectonic implications. Chinese J Geophys. 2022;65:1980–90. https://doi.org/10.6038/cjg2022P0173.
Ma XB, Kong XR, Liu HB, Yan YL. The electrical structure of northeastern Qinghai_Tibet plateau. Chin J Geophys. 2005;48:689–97. https://doi.org/10.1002/cjg2.710.
McKenzie D, Jackson J, Priestley K. Thermal structure of oceanic and continental lithosphere. Earth Planet Sci Lett. 2005;233:337–49. https://doi.org/10.1016/j.epsl.2005.02.005.
Miensopust MP, Jones AG, Hersir GP, Vilhjálmsson AM. The Eyjafjallajökull volcanic system, Iceland: insights from electromagnetic measurements. Geophys J Int. 2014;199:1187–204. https://doi.org/10.1093/gji/ggu322.
Pan JT, Li YH, Wu QJ, Ding ZF, Yu DX. Phase velocity maps of Rayleigh wave based on a dense coverage and portable seismic array in NE Tibetan plateau and its adjacent regions. Chin J Geophys. 2017;60:2291–303. https://doi.org/10.6038/cjg20170621.
Pan ZY, Zhou Y, Zhao GQ. Contemporary crustal deformation within northeast Tibet constraint from 3-dimensional GPS strain analysis based on the green function of elastic thin sheet. J Geod Geodyn. 2020;40:351–6. https://doi.org/10.14075/j.jgg.2020.04.005.
Patro PK. Magnetotelluric studies for hydrocarbon and geothermal resources: examples from the Asian Region. Surv Geophys. 2017;38:1005–41. https://doi.org/10.1007/s10712-017-9439-x.
Paul WJ, Glover A, Malcolm JH, Jaume PB. A modified Archie's law for two conducting phases. Earth Planet Sci Lett. 2000;180:369–83. https://doi.org/10.1016/S0012-821X(00)00168-0.
Pavez M, Diaz D, Brasse H, Kapinos G, Budach I, Goldberg V, Morata D, Schill E. Shallow and deep electric structures in the Tolhuaca geothermal system (S. Chile) investigated by Magnetotellurics. Remote Sens. 2022;14:6144. https://doi.org/10.3390/rs14236144.
Peacock JR, Thiel S, Reid P, Heinson G. Magnetotelluric monitoring of a fluid injection: example from an enhanced geothermal system. Geophys Res Lett. 2012;39:L18403. https://doi.org/10.1029/2012GL053080.
Pinã VP, Ledo J, Queralt P, Marcuello A, Bellmunt F, Hidalgo R, Messeiller M. 3-D Magnetotelluric exploration of tenerife geothermal system (Canary Islands, Spain). Surv Geophys. 2014;35:1045–64. https://doi.org/10.1007/s10712-014-9280-4.
Priestley K, Kenzie DM. The thermal structure of the lithosphere from shear wave velocities. Earth Planet Sci Lett. 2006;244:285–301. https://doi.org/10.1016/j.epsl.2006.01.008.
Replumaz A, Tapponnier P. Reconstruction of the deformed collision zone between India and Asia by backward motion of lithospheric blocks. J Geophys Res: Solid Earth. 2003;108:2285. https://doi.org/10.1029/2001JB000661.
Shen ZK, Wang M, Li YX, Jackson DD, Yin A, Dong DN, Fang P. Crustal deformation along the Altyn Tagh fault system, western China, from GPS. J Geophys Res. 2001;106:30607–21. https://doi.org/10.1029/2001JB000349.
Shi BY, Zhang JT. Discussion on the Gap of Qin-Kun tectonic belt. Manag Strategy Qinghai Land Resour. 1982;3:21–9.
Silver PG. Seismic anisotropy beneath the continents: probing the depths of geology. Annu Rev Earth Planet Sci. 1996;24:385–432. https://doi.org/10.1146/annurev.earth.24.1.385.
Spichak VV, Zakharova OK, Goidina AG. 3D temperature model of the Hengill geothermal area (Iceland) revealed from electromagnetic data. In; proceedings, Thirty-Sixth Workshop on Geothermal Reservoir Engineering Stanford University, Stanford, California. 2011. SGP-TR-191.
Su Q, Xie H, Yuan DY, Zhang HP. Along-strike topographic variation of Qinghai Nanshan and its significance for landscape evolution in the northeastern Tibetan Plateau. J Asian Earth Sci. 2017;147:226–39. https://doi.org/10.1016/j.jseaes.2017.07.019.
Sun J, Jin GW, Bai DH, Wang LF. Sounding of electrical structure of the crust and upper mantle along the eastern border of Qinghai Tibetan Plateau and its tectonic significance. Sci Chin (series d). 2003;46:243–53.
Sun Y, Niu F, Liu HF, Chen YL, Liu JX. Crustal structure and deformation of the SE Tibetan plateau revealed by receiver function data. Earth Planet Sci Lett. 2012;349:186–97. https://doi.org/10.1016/j.epsl.2012.07.007.
Tan H, Ling F, Guo Z, Li J, Liu J. Application of a wide-field electromagnetic method for hot dry rock exploration: a case study in the Gonghe Basin, Qinghai. Chin Miner. 2021;11:1105. https://doi.org/10.3390/min11101105.
Tang XC, Wang GL, Ma Y, Zhang DL, Liu Z, Zhao X, Cheng TJ. Geological model of heat source and accumulation for geothermal anomalies in the Gonghe basin, northeastern Tibetan Plateau. Acta Geol Sin. 2020;94:2052–65. https://doi.org/10.3969/j.issn.0001-5717.2020.07.013.

Tapponnier P, Xu ZB, Roger F, Meyer B, Arnaud N, Wittlinger G, Yang JS. Oblique stepwise rise and growth of the Tibet Plateau. Science. 2001;294:1671–7. https://doi.org/10.1126/science.105978.
Unsworth MJ, Jones AG, Wei W, Marquis G, Gokarn SG, Spratt JE, the INDEPTH-MT Team. Crustal rheology of the Himalaya and southern Tibet inferred from magnetotelluric data. Nature. 2005;438:78–81. https://doi.org/10.1038/nature04154.
Wang XS, Fang J, Hsu HT. 3D density structure of lithosphere beneath northeastern margin of the Tibetan Plateau. Chinese J Geophys. 2013;56:3770–8. https://doi.org/10.6038/cjg20131118.
Wang HY, Gao R, Li QS, Li WH, Hou HS, Kuang CY, Xue AM, Huang WY. Deep seismic reflection profiling in the Songpan-west Qinling-Linxia basin of the Qinghai-Tibet plateau: data acquisition, data processing and preliminary interpretations. Chin J Geophys. 2014;57:1451–61. https://doi.org/10.6038/~g20140510.
Wang Q, Niu F, Gao Y, Chen YT. Crustal structure and deformation beneath the NE margin of the Tibetan plateau constrained by teleseismic receiver function data. Geophys J Int. 2016a;204:167–79. https://doi.org/10.1093/gji/ggv420.
Wang Q, Hawkesorth CJ, Wyman D, Chung SL, Wu FY, Li XH, Li ZX, Gou GN, Zhang XZ, Tang GJ, Dan W, Ma L, Dong YH. Pliocene-Quaternary crustal melting in central and northern Tibet and insights into crustal flow. Nat Commun. 2016b;7:11888. https://doi.org/10.1038/ncomms11888.
Wang XB, Yu N, Gao S, Luo W, Cai XL. Research progress in research on electrical structure of crust and upper mantle beneath the eastern margin of the Tibetan plateau. Chinese J Geophys. 2017;60:2350–70. https://doi.org/10.6038/cjg20170626.
Wang Y, Yuan XC, Zhang YH, Zhang X, Xiao Y, Duo J, Huang X, Sun ML, Lv GS. Hydrochemical, D-O–Sr isotopic and electromagnetic characteristics of geothermal waters from the Erdaoqiao area, SW China: insights into genetic mechanism and scaling potential. Ore Geol Rev. 2023;158:105486. https://doi.org/10.1016/j.oregeorev.2023.105486.
Wei WB, Jin S, Ye GF, Deng M, Tan HD, Unsworth M, Jones AG, Book J, Li SH. Conductivity structure of crust and upper mantle beneath the northern Tibetan Plateau: results of super wide band magnetotelluric sounding. Chin J Geophys. 2006;49:1215–25. https://doi.org/10.1002/cjg2.933.
Wei W, Le Pape FL, Jones AG, Vozar J, Dong H, Unsworth MJ, Jin S, Ye GF, Jing JE, Zhang LT, Xie CL. Northward channel flow in northern Tibet revealed from 3D magnetotelluric modelling. Phys Earth Planet Inter. 2014;235:13–24. https://doi.org/10.1016/j.pepi.2014.07.004.
Xia SR, Shi L, Li YH, Guo LH. Velocity structure of the crust and uppermost mantle beneath the northeast margin of the Tibetan plateau revealed by double-difference tomography. Chinese J Geophys. 2021;64:3194–206. https://doi.org/10.6038/cjg2021O0514.
Xiao Z, Gao Y. Crustal velocity structure beneath the northeastern Tibetan plateau and adjacent regions derived from double difference tomography. Chinese J Geophys. 2017;60:2213–25. https://doi.org/10.6038/cjg20170615.
Xiao QB, Zhang J, Zhao GZ, Wang JJ. Electrical resistivity structures northeast of the Eastern Kunlun fault in the Northeastern Tibet: tectonic implications. Tectonophysics. 2013;601:125–38. https://doi.org/10.1016/j.tecto.2013.05.003.
Xiong SQ, Di YY, Li ZK. Characteristics of China continent magnetic basement depth. Chin J Geophys. 2014;57:3981–93. https://doi.org/10.6038/cjg20141211.
Xu ZQ, Yang JS, Ji SC, Zhang ZM, Li HB, Liu FL, Zhang JX, Wu CL, Li ZH, Liang FH. On the continental tectonics and dynamics of China. Acta Geol Sin. 2010;84:1–29.
Xu TF, Hu ZX, Li ST, Jiang ZJ, Hou ZY, Li FY, Liang X, Feng B. Enhanced geothermal system: international progresses and research status of China. Acta Geol Sin. 2018;92:1936–47. https://doi.org/10.3969/j.issn.0001-5717.2018.09.012.
Xue GQ, Qian H, Jiang M, Sun HP, Dong YJ. Studies on the velocity structure of crust-upper mantle beneath Northeast Qinghai-Tibet Plateau. China Acta Geoscientia Sinica. 2003;24:19–26.
Yan WD. Characteristics of Gonghe Basin hot dry rock and its utilization prospects. Sci Technol Rev. 2015;33:54–7. https://doi.org/10.3981/j.issn.1000-7857.2015.19.008.
Yang HW, Shen JF, Wei LY, Zhang Z, Liu MN, Feng BX, Zhang LN. Zircon U-Pb ages, geochemical characteristics and tectonic implications of Xigongka granodiorite around Gonghe Basin, west of Western Qinling Mountains. Geoscience. 2018;32:316–28. https://doi.org/10.19657/j.geoscience.1000-8527.2018.02.10.
Ye T, Huang QH, Chen XB, Zhang HQ, Chen YJ, Zhao L, Zhang Y. Magma chamber and crustal channel flow structures in the Tengchong volcano area from 3-D MT inversion at the intracontinental block boundary southeast of the Tibetan Plateau. J Geophys Res: Solid Earth. 2018a;123:11112–26. https://doi.org/10.1029/2018JB015936.
Ye Z, Gao R, Li QS, Xu X, Huang XF, Xiong XS, Li WH. Eastward extrusion and northward expansion of the Tibetan Plateau-discussions for the deep processes of the plateau uplift. Chin Sci Bull. 2018b;63:3217–28. https://doi.org/10.1360/N972018-00478.
Yuan DY, Ge WP, Chen ZW, Li CY, Wang ZC, Zhang HP, Zhang PZ, Zheng DW, Zheng WJ, Craddock WH, Dayem KE, Duvall AR, Hough BG, Lease RO, Champagnac JD, Burbank DW, Clark MK, Farley KA, Garzione CN, Kirby E, Molnar P, Roe GH. The growth of northeastern Tibet and its relevance to large-scale continental geodynamics: a review of recent studies. Tectonics. 2013;32:1358–70.
Yun XR, Chen XJ, Cai ZH, He BZ, Zhang SS, Lei M, Xiang H. Preliminary study on magmatic emplacement and crystallization conditions and deep structure of hot dry rock in the northeastern Gonghe basin Qinghai Province. Acta Petrologica Sinica. 2020;36:3171–91. https://doi.org/10.18654/1000-0569/2020.10.14.
Zhang GW, Guo AL, Yao AP. Western Qinling-Songpan continental tectonic node in China's continental tectonics. Earth Sci Front. 2004;11:23–32. https://doi.org/10.3321/j.issn:1005-2321.2004.03.004.
Zhang HF, Chen YL, Xu WC, Liu R, Yuan HL, Liu XM. Granitoids around Gonghe basin in Qinghai province: petrogenesis and tectonic implications. Acta Petrologica Sinica. 2006;22:2910–22. https://doi.org/10.3321/j.issn:1000-0569.2006.12.009.
Zhang X, Jia S, Zhao J, Zhang C, Yang J, Wang F, Zhang J, Liu B, Sun G, Pan NS. Crustal structures beneath west Qinling-east Kunlun Orogen and its adjacent area-result of wide-angle seismic reflection and refraction experiment. Chin J Geophys. 2008;51:307–18. https://doi.org/10.3321/j.issn:0001-5733.2008.02.016.
Zhang ZJ, Klemperer S, Bai ZM, Chen Y, Teng JW. Crustal structure of the Paleozoic Kunlun orogeny from an active-source seismic profile between Moba and Guide in East Tibet China. Gondwana Res. 2011;19:994–1007.

Zhang C, Zhang SS, Li ST, Jia XF, Jiang GZ, Gao P, Wang YB, Hu SB. Geothermal characteristics of the Qiabuqia geothermal area in the Gonghe basin. Chinese J Geophys. 2018a;61:4545–57. https://doi.org/10.6038/q92018L0747.
Zhang SQ, Yan WD, Li DP, Jia XF, Zhang SS, Li ST, Fu L, Wu HD, Zeng ZF, Li ZW, Mu JQ, Cheng ZP, Hu LS. Characteristics of geothermal geology of the Qiabuqia HDR in Gonghe Basin, Qinghai Province. Geology in China. 2018b;45:1087–102. https://doi.org/10.12029/gc20180601.
Zhang SS, Zhang L, Tian CC, Cai JS, Tang BC. Occurrence geological characteristics and development potential of hot dry rocks in Qinghai Gonghe Basin. J Geomech. 2019;25:501–8. https://doi.org/10.12090/j.issn.1006-6616.2019.25.04.048.
Zhang SQ, Li XF, Song J, Wen DG, Li ZW, Li DP, Cheng ZP, Fu L, Zhang LY, Feng QD, Yang T, Niu ZX. Analysis on the geophysical evidence for the existence of partial melting layer in the crust and the regional heat source mechanism for the hot dry rock resources of the Gonghe basin. Earth Sci. 2021;46:1416–36. https://doi.org/10.3799/dqkx.2020.094.
Zhao XY, Zeng ZF, Huai N, Wang K. Geophysical responses and possible geothermal mechanism in the Gonghe Basin China. Geomech Geophys Geo-Energ Geo-Resour. 2020;6:6–17. https://doi.org/10.1007/s40948-020-00141-5.
Zheng QS. Comprehensive study on Qinghai earthquake. Beijing: Seismological Press; 1999.
Zheng G, Wang H, Wright TJ, Lou Y, Zhang R, Zhang WX, Shi C, Huang JF, Wei N. Crustal deformation in the India-Eurasia collision zone from 25 years of GPS measurements. J Geophys Res. 2017;122:9290–312. https://doi.org/10.1002/2017JB014465.
Zhou MD, Wang CR, Zeng RS. Seismic tomography of the velocity structure of the crust and upper Mantle in Northeastern Margin of the Qinghai-Tibet Plateau. Northwest Seismol J. 2012;3:224–33. https://doi.org/10.3969/j.issn.1000-0844.2012.03.0224.

Publisher's Note